Ultrabroadband infrared nanospectroscopic imaging

Hans A. Bechtel[a,1], Eric A. Muller[b,c,d], Robert L. Olmon[b,c,d], Michael C. Martin[a,1], and Markus B. Raschke[b,c,d,1]

[a]Advanced Light Source Division, Lawrence Berkeley National Laboratory, Berkeley, CA 94720; Departments of [b]Physics and [c]Chemistry, University of Colorado, Boulder, CO 80309; and [d]JILA, University of Colorado and National Institute of Standards and Technology, Boulder, CO 80309

Edited by Richard P. Van Duyne, Northwestern University, Evanston, IL, and approved April 4, 2014 (received for review January 12, 2014)

Characterizing and ultimately controlling the heterogeneity underlying biomolecular functions, quantum behavior of complex matter, photonic materials, or catalysis requires large-scale spectroscopic imaging with simultaneous specificity to structure, phase, and chemical composition at nanometer spatial resolution. However, as with any ultrahigh spatial resolution microscopy technique, the associated demand for an increase in both spatial and spectral bandwidth often leads to a decrease in desired sensitivity. We overcome this limitation in infrared vibrational scattering-scanning probe near-field optical microscopy using synchrotron midinfrared radiation. Tip-enhanced localized light–matter interaction is induced by low-noise, broadband, and spatially coherent synchrotron light of high spectral irradiance, and the near-field signal is sensitively detected using heterodyne interferometric amplification. We achieve sub-40-nm spatially resolved, molecular, and phonon vibrational spectroscopic imaging, with rapid spectral acquisition, spanning the full midinfrared (700–5,000 cm^{-1}) with few cm^{-1} spectral resolution. We demonstrate the performance of synchrotron infrared nanospectroscopy on semiconductor, biomineral, and protein nanostructures, providing vibrational chemical imaging with subzeptomole sensitivity.

nano-FTIR | chemical identification | bioimaging

Many properties and functions of natural or synthetic materials are defined by chemically or structurally distinct phases, domains, or interfaces on length scales of a few nanometers to micrometers. Characterizing these heterogeneities has long driven the development of advanced microscopy techniques, with notable advances in electron (1), photoemission (2), X-ray (3), and superresolution (4) microscopies. Although extremely effective, these techniques have strict sample requirements: either they operate in vacuum, are limited by electron or X-ray beam damage, or rely on labeling with exogenous fluorophores.

In contrast, infrared (IR) vibrational spectroscopic imaging is minimally invasive, requires little sample preparation, is applicable in situ and under ambient conditions, and provides intrinsic chemical contrast and spectroscopic identification for a wide range of materials (5), including living cells (6) and tissues (7, 8). The spatial resolution, however, is diffraction-limited to 2–10 μm, depending on wavelength. Moreover, high signal-to-noise spectra even at this low resolution are only possible with a source of high spectral irradiance (9). Subwavelength imaging has been achieved to some extent through point-spread function deconvolution (10, 11) and attenuated total reflection techniques (12). However, the micrometer-size wavelength of IR radiation, in general, has fundamentally limited its application for the characterization of essentially any mesoscopic, heterogeneous material where chemical information at the nanoscale is desired.

Infrared scattering-scanning near-field microscopy (IR *s*-SNOM) overcomes the diffraction limit by scattering incident light with the typically metallic tip of an atomic force microscope (AFM) scanning in nanometer proximity to the sample (13, 14). The conductive tip effectively acts as an optical antenna by localizing and scattering the IR optical field in the near-field region of its nanoscopic apex. Consequently, the spatial resolution of *s*-SNOM is independent of the incident IR wavelength and is determined to first approximation only by the radius of the tip apex, which is typically 10–20 nm.

IR *s*-SNOM nanospectroscopy and imaging with chemical contrast, however, has not yet achieved its full potential in terms of versatility and spectral coverage compared with conventional Fourier transform infrared (FTIR) techniques. Lasers are typically used as *s*-SNOM sources because they provide the high spectral irradiance that is necessary to obtain detectable signal levels from the nanoscopic probe volumes arising from the intrinsic high spatial resolution. Narrow-band continuous wave (CW) tunable IR lasers offer the highest spectral irradiance, but nanoscale spectroscopy can only be performed over the typically narrow tuning range of these lasers, which cover ∼1 vibrational mode (13, 14). Femtosecond-pulsed IR lasers, which trade both spectral irradiance and total power for increased spectral bandwidth, enable the investigation of one or multiple vibrational modes without tuning (15–17). Broadband and continuum sources have achieved bandwidths suitable for investigation of a significant portion of the IR region (18, 19), although the combination of sufficient power across the full mid-IR at high repetition rates remains difficult. Thus, the bandwidth of the broadest IR laser sources yet implemented for *s*-SNOM is only a fraction of the full IR range provided by a thermal source in conventional FTIR. For both CW and femtosecond-pulsed laser sources, the spectral tuning required to cover a broader spectral range necessarily makes the experiment prone to laser and sample drift, thereby limiting the spectral quality that can be obtained in *s*-SNOM.

Heated filament or globar sources, which are the standard FTIR sources, have been implemented in *s*-SNOM investigations (20), but despite the large total flux, the extremely low spectral irradiance arising from the lack of spatial coherence in these

Significance

Through direct measurement of intrinsic vibrational and electronic modes, infrared spectroscopy provides label-free, chemical characterization of molecules and solids. The long micrometer-sized wavelength of infrared light, however, has limited the application of this widely applied spectroscopic technique to ensemble studies, preventing nanoscale spatially resolved spectroscopy of heterogeneous materials. We overcome this limitation by combining scattering-scanning near-field optical microscopy with broadband infrared synchrotron radiation. Using this synchrotron infrared nanospectroscopy (SINS) technique, we achieve spectroscopic imaging over the entire midinfrared with nanometer spatial resolution and high sensitivity. With a spatial resolution 100–1,000 times better than conventional FTIR microscopy, SINS enables the investigation of nanoscale phenomena in soft matter, even under ambient and environmental conditions that are essentially inaccessible by other techniques.

Author contributions: H.A.B., E.A.M., R.L.O., M.C.M., and M.B.R. designed research; H.A.B., E.A.M., and R.L.O. performed research; H.A.B., E.A.M., R.L.O., M.C.M., and M.B.R. analyzed data; and H.A.B., E.A.M., M.C.M., and M.B.R. wrote the paper.

The authors declare no conflict of interest.

This article is a PNAS Direct Submission.

[1]To whom correspondence may be addressed. E-mail: habechtel@lbl.gov, mcmartin@lbl.gov, or markus.raschke@colorado.edu.

This article contains supporting information online at www.pnas.org/lookup/suppl/doi:10.1073/pnas.1400502111/-/DCSupplemental.

sources severely limits signal levels. An alternative technique, thermal IR near-field spectroscopy, uses a heated tip or sample to directly image in the thermal near field and takes advantage of the enhanced local density of states as well as the improved spatial coherence of the tip-scattered light relative to a conventional blackbody source (21, 22). However, even in this case, the signal strength remains weak and additional complications abound with sample melting and scanning at high tip temperatures.

Synchrotron IR radiation, in contrast, is spectrally broad, bright, and spatially coherent, overcoming the above limitations with a spectral irradiance 1,000 times higher than a thermal source and a spectral bandwidth well over 10 times that of the broadest laser sources (Fig. 1*A*) (23). The suitability of synchrotron IR radiation for near-field spectroscopy and imaging has been recognized previously (24–26), but the bandwidth and spatial coherence of the source have not been fully used. The spatial coherence and high spectral irradiance enable diffraction-limited focusing, resulting in improved coupling of the incident light to the AFM tip. Furthermore, the spatial coherence allows for efficient optical heterodyne signal amplification and phase-resolved detection. The short- and long-term stability of the synchrotron also enables low-noise spectroscopy and the possibility for efficient signal averaging, whereas walk-up operation and minimal sample preparation allow the apparatus to act as part of a user facility.

In this work, we develop synchrotron infrared nanospectroscopy (SINS) as a tool for nanoscale FTIR spectroscopy. We demonstrate sub-40-nm spatial resolution FTIR spectroscopy covering the full mid-IR absorption region 700–5,000 cm^{-1} (13–2 μm). We show high-resolution, broad-bandwidth SINS spectra in the investigation of a surface phonon polariton in SiO_2, the identification of $CaCO_3$ biomineral polymorphs through characteristic vibrational modes, and an analysis of surface-adsorbed dried proteins, containing spectral information on protein structure and identity. Complete mid-IR spanning spectra can be acquired in a few seconds, and images with chemically sensitive IR vibrational contrast are collected on a timescale of minutes. This allows chemical identification across the full IR range, with simultaneous high spectral resolution enabling the distinction between different local chemical environments, phases, or morphologies.

Experiment

IR synchrotron radiation is provided by the Advanced Light Source (ALS) at Lawrence Berkeley National Laboratory. IR light is focused onto the apex of an oscillating platinum silicide (Nanosensors, PTSi–NCH) or platinum-coated silicon (Nanoworld, ARROW-NCPt) tip of a specially modified AFM (Innova, Bruker) (Fig. 1*B* and Fig. S1). The tip oscillation at frequency ω_t induces harmonics in the near-field scattered signal due to the nonlinear distance dependence of the near-field tip–sample interaction (27, 28). This allows for discrimination of the near-field signal from the weakly spatially dependent far-field background that originates from the tip shaft and sample, by detection at higher harmonics of ω_t with a lock-in amplifier. The near-field spectra are referenced against a spectrally flat near-field response from a gold or silicon surface to eliminate the instrument response function (Fig. S2). The 700–5,000-cm^{-1} spectral range of the instrument in the current implementation is only limited by the response of the mercury cadmium telluride (MCT) detector and KBr beamsplitter. The mid-IR region is of greatest interest for chemical identification; however, the range at this beamline endstation can be easily extended into the terahertz (THz) (<700 cm^{-1}) or near-IR (>5,000 cm^{-1}) regions with a different detector–beamsplitter combination. In general, THz to extreme UV *s*-SNOM is possible with synchrotron radiation at the respective beamlines optimized for these spectral ranges.

Spectrally integrated IR images are obtained simultaneously with the topography by self-homodyne detection. For SINS point, line, and area spectroscopy at selected sample locations, we perform interferometric heterodyne detection. Akin to dispersive Fourier transform spectroscopy (29), free-induction decay *s*-SNOM (15), and nano-FTIR (17, 20), we use an asymmetric Michelson interferometer to frequency resolve the scattered near-field signal and amplify the weak, tip-scattered light. Unlike previous implementations of broadband *s*-SNOM, we use a modified commercial FTIR spectrometer (Nicolet 6700, Thermo-Scientific) to take advantage of the rapid-scan capabilities. The Fourier transform of the interferogram results in the complex-valued near-field spectrum. The real $\mathrm{Re}(\bar{\nu})$ and imaginary $\mathrm{Im}(\bar{\nu})$ spectra, typically represented as spectral amplitude $|A(\bar{\nu})|$ and phase $\Phi(\bar{\nu})$, relate to the complex dielectric function of the material (15, 30). Referencing the near-field spectra to a nonresonant or spectrally flat substrate thus enables determination of the frequency-dependent optical constants of the material (30).

Results

SiO_2 Surface Phonon Polariton. Fig. 2*A* shows interferograms acquired with the tip on Si and SiO_2, respectively. Si has a flat spectral response in the mid-IR, resulting in a wavelength-

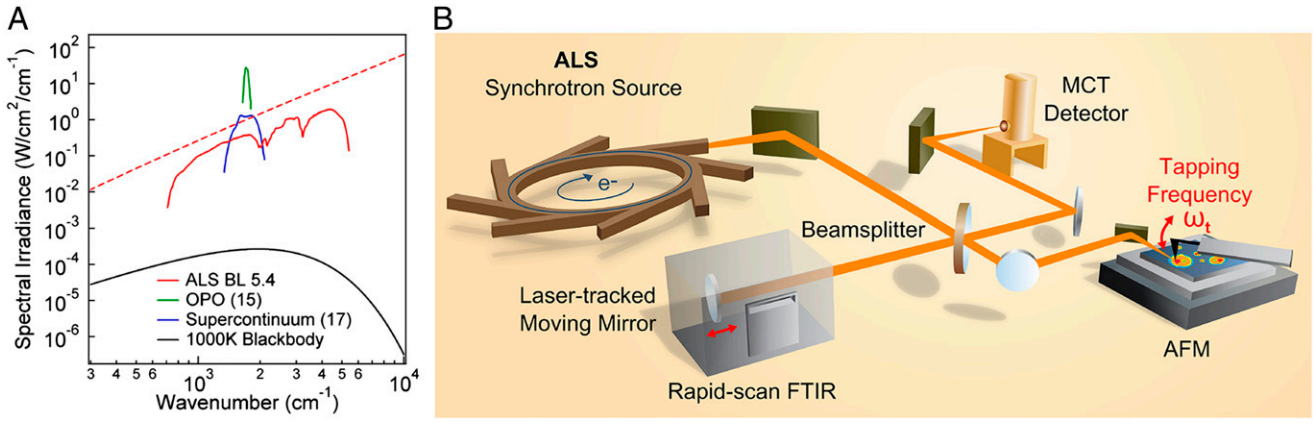

Fig. 1. *s*-SNOM with a synchrotron infrared source. (*A*) Spectral irradiance and bandwidth achievable in a single acquisition for *s*-SNOM-implemented broadband IR sources: IR synchrotron light from ALS Beamline 5.4 (calculated, red-dashed; experimental detector-limited, red-solid), an optical parametric oscillator (OPO) laser source (green) (15), a supercontinuum laser source (blue) (17), and a 1,000-K blackbody source (black). Note that the center frequency of the laser sources can be tuned to cover additional spectral regions (600 – 2,500 cm^{-1}). (*B*) Optical layout of the SINS experiment with ALS Beamline 5.4 as the broadband IR synchrotron source.

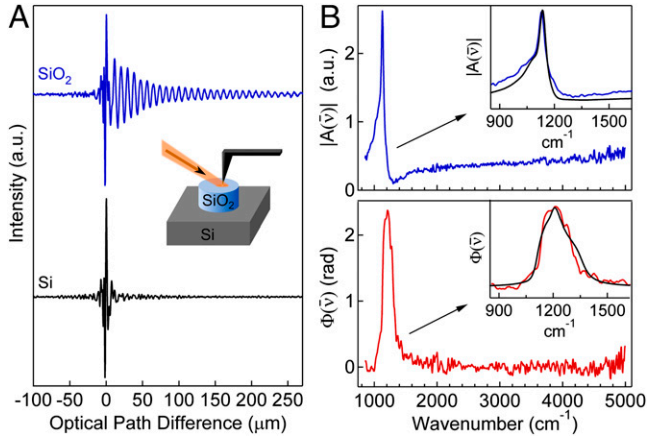

Fig. 2. SiO_2 surface phonon polariton. (*A*) Partial SINS interferograms around the zero path difference point recorded on SiO_2 (blue) and Si (black), detected at $2\omega_t$. (*Inset*) Tip–sample geometry of 100-nm-thick SiO_2 microstructure on Si. (*B*) SINS amplitude $|A(\bar{\nu})|$ (blue) and phase $\Phi(\bar{\nu})$ (red) spectra of SiO_2 referenced to Si at 8-cm^{-1} spectral resolution, processed from the two interferograms in *A*. (*Insets*) Zoom-in on SiO_2 surface phonon polariton mode showing the experimental SINS $|A(\bar{\nu})|$ (blue) and $\Phi(\bar{\nu})$ (red) spectra with calculated spectra (black) from a point-dipole model.

independent scattering amplitude and a flat spectral phase. The scattered near-field signal thus has a spectral distribution similar to the incident light, and the interferogram is observed to be symmetric with a short coherence length, as expected for broadband radiation. SiO_2, on the other hand, has a strong phonon resonance, which produces an asymmetric interferogram. The asymmetry resembles free-induction decay signals in coherent femtosecond spectroscopy, including free-induction decay *s*-SNOM. In SINS, however, the asymmetry is caused by frequency-dependent $|A(\bar{\nu})|$ and $\Phi(\bar{\nu})$ in the scattered light, resulting in the long coherence observed in the cross-correlation interferogram.

The Fourier transform of the signal (Fig. 2*B*) reveals a sharp peak at 1,130 cm^{-1} in the $|A(\bar{\nu})|$ spectrum and a broad peak near 1,215 cm^{-1} in the $\Phi(\bar{\nu})$ spectrum, with a high signal-to-noise ratio across the mid-IR region from 700 to 5,000 cm^{-1}. Additionally, we observe a low-energy shoulder and smaller high-energy shoulder in $|A(\bar{\nu})|$ (Fig. 2*B*, *Inset*), as seen in previous *s*-SNOM investigations (16, 31). These features are due to the SiO_2 surface phonon polariton mode (14, 32), which is caused by strong coupling of light to dispersive phonon modes in the 1,000 – 1,300 cm^{-1} range. In the presence of a conductive AFM tip, the spectral shape is highly dependent upon near-field tip–sample coupling that manifests itself experimentally with spectra sensitive to changes in AFM tip characteristics, tapping parameters, and lock-in detection. We qualitatively model the spectra with the established point-dipole model (28, 33), using literature values for the dielectric constants of the sample (34) and tip (35), experimentally measured tip radii of 20–40 nm, and a cantilever tapping amplitude of 50 nm. These results show good agreement with the experimental spectra. However, to extract the exact real and imaginary components of the material dielectric constant, more complicated models of the tip polarizability must be considered, as described in detail elsewhere (30, 31, 36).

Fig. 3 *A* and *B* shows the topography and broadband SINS images of an ~100-nm-thick SiO_2 microstructure on Si. Imaging contrast between the two materials integrated across this broad spectral range is primarily nonresonant and mostly represents the change in the nonresonant offset of the dielectric permittivity ϵ_1 between Si and SiO_2. Profiles extracted from these images show the spatial resolution to be better than 40 nm for the infrared signal (Fig. 3*B*, *Inset*).

Spectrally resolved linescans of $|A(\bar{\nu})|$ and $\Phi(\bar{\nu})$ (Fig. 3 *C* and *D*) across the step edge show the evolution of the SiO_2 surface phonon polariton mode as the prominent feature. Fig. 3 *E* and *F* displays individual spectra at 16-cm^{-1} resolution obtained within SiO_2, at the edge of the structure, and on the silicon substrate. Increasing *s*-SNOM intensity is observed across the step edge both in the spectrally integrated response as well as in the spectrally resolved $\Phi(\bar{\nu})$ and $|A(\bar{\nu})|$ data. This increase results from both the thickness-dependent dielectric function of SiO_2 and the average effective medium dielectric constant probed by the evanescent field of the tip at the edge. The spectrally resolved linescans also reveal spectral shifts at the SiO_2 edge (Fig. 3 *E* and *F*), which may be attributed to changes in the SiO_2 thickness that have been shown to cause spectral shifts (31) and/or changes in the interaction geometry. (The spectra of a strongly resonant surface phonon polariton are known to be highly dependent on details of the tip–sample interaction. The sharp edges of the SiO_2 microstructure alter the tip–sample coupling and illumination that can result in shifts in the measured spectra.)

$CaCO_3$ Polymorph Heterogeneity in a *Mytilis edulis* Shell. As a second example, we demonstrate the applicability of SINS toward the study of calcium carbonate ($CaCO_3$) polymorph heterogeneity in a natural biological system. Like many bivalves, blue mussels (*M. edulis*) form a bimineralic shell that transitions during growth from calcite to aragonite as influenced by a number of environmental parameters (37). Fig. 4 shows AFM topography and SINS spectra from a polished *M. edulis* mollusk shell in the interface region between the outer calcite and inner aragonite (nacre) layers. The AFM topography (Fig. 4*A*) illustrates the different morphological structures of the two polymorphs, with the calcite crystals (Fig. 4*A*, *Left*) formed in large, irregular shapes and the aragonite (Fig. 4*A*, *Right*) crystals formed in polygonal tablets with widths of a few hundred nanometers.

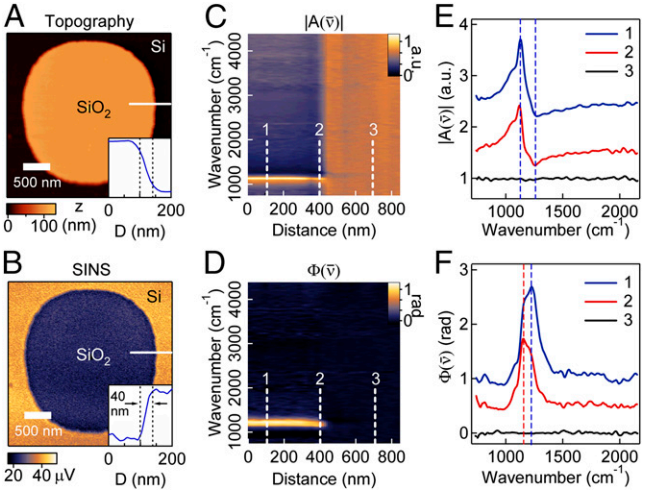

Fig. 3. SiO_2 microstructures on Si. (*A*) AFM topography and (*B*) simultaneously recorded broadband SINS image. (*Insets*) Profiles of topography and IR response across the SiO_2 edge, as indicated by the white line in *A* and *B*, respectively. The distance between the dashed black lines is 40 nm. Spatio-spectral SINS linescan of (*C*) $|A(\bar{\nu})|$ and (*D*) $\Phi(\bar{\nu})$ along the white line in *A* and *B*. Each of the 30 spectra in the plot was acquired for 1 min at 16-cm^{-1} spectral resolution. SINS (*E*) $|A(\bar{\nu})|$ and (*F*) $\Phi(\bar{\nu})$ spectra at three locations along the linescan in *C* and *D*. The position 1 spectra (blue) are offset for clarity by 2 and 1 in *E* and *F*, respectively, and the position 2 spectra (red) are offset by 1 and 0.5 in *E* and *F*, respectively. In *E*, the dashed lines are the maximum (1,130 cm^{-1}) and minimum (1,264 cm^{-1}) of the position 1 spectra, and in *F* the dashed lines are the peak positions of the position 1 (1,225 cm^{-1}) and position 2 (1,155 cm^{-1}) spectra.

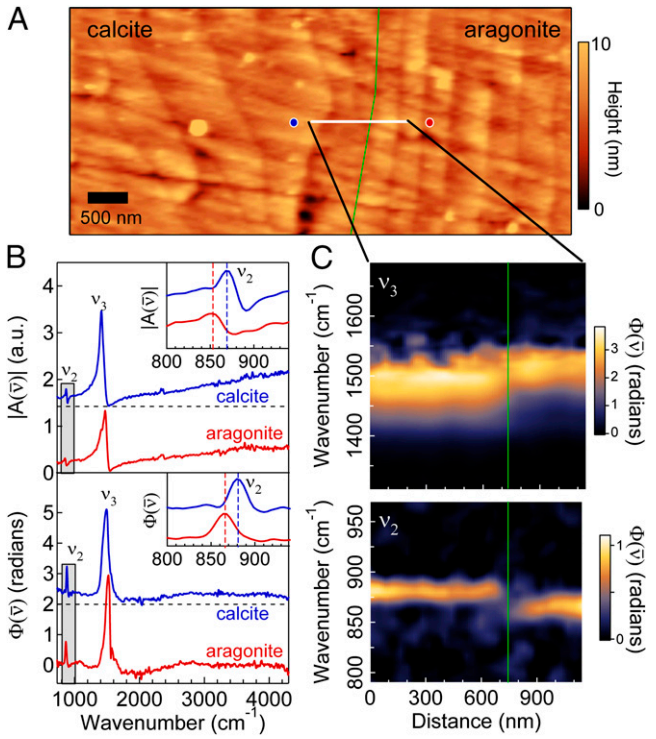

Fig. 4. $CaCO_3$ polymorph heterogeneity in a polished *M. edulis* shell. (*A*) AFM topography in the interface region of calcite (*Left*), appearing with a globular morphology, and aragonite (*Right*), appearing as stacked tablets. The green line indicates the interface between calcite and aragonite. (*B*) SINS $|A(\bar{\nu})|$ and $\Phi(\bar{\nu})$ spectra of calcite (blue, offset for clarity) and aragonite (red) at 8-cm^{-1} spectral resolution acquired at the location of the blue and red circles, respectively, in *A*. (*Insets*) Zoom-in of ν_2 mode (gray box) for calcite (blue) and aragonite (red) with the dashed lines indicating the peak positions. (*C*) Spatio-spectral SINS linescan $\Phi(\bar{\nu})$ plot across the solid white line in *A*. Each of the 30 spectra was acquired for 3 min at 8-cm^{-1} spectral resolution.

As shown in Fig. 4*B*, SINS $|A(\bar{\nu})|$ and $\Phi(\bar{\nu})$ spectra of calcite and aragonite readily distinguish the two $CaCO_3$ polymorphs through the frequency of the $CaCO_3$ vibrational modes in each material (38). Two vibrational modes localized on the CO_3^{2-} ion, namely the out-of-plane bending ν_2 and the doubly degenerate asymmetric stretching ν_3 modes, have IR vibrational resonances at different frequencies in each polymorph. The bandwidth of the synchrotron source allows both modes to be resolved simultaneously. Moreover, the broad bandwidth enables the assessment of any sample contamination, adsorbed water, or additional biominerals, such as apatite (39), that might have features in other spectral areas. The $\Phi(\bar{\nu})$ spectra indicate that the ν_2 mode (Fig. 4*B*, *Inset*) in orthorhombic aragonite (880 cm^{-1}) is observed at lower frequencies relative to that in trigonal calcite (865 cm^{-1}), as expected and in agreement with laser-based *s*-SNOM (39), whereas the ν_3 mode in aragonite (1,520 cm^{-1}) is resonant at a higher frequency relative to the calcite (1,495 cm^{-1}). Although the ν_3 mode is stronger and has a larger difference ($\sim$30 cm^{-1}) in resonant frequency between the two materials, the vibrational shift is more evident for the ν_2 mode due to its narrower linewidth. Fig. 4*C* shows a spatio-spectral linescan of the interface region along the solid, white line in Fig. 4*A*. The ν_2 mode, in particular, reveals the sharp transition between calcite and aragonite, consistent with previous electron (40) and X-ray microscopy (41) investigations.

Surface-Absorbed Dried Proteins and Peptoid Nanosheets. SINS is minimally invasive and allows for the nondestructive study of soft matter, including synthetic- and biopolymers. IR *s*-SNOM has recently been used for investigating protein organization and morphology, including membrane proteins (13, 42). The strongest vibrational signature of proteins arise from the Amide I (typical center frequency 1,620–1,700 cm^{-1}) and Amide II (1,500–1,560 cm^{-1}) modes, which have been previously used to identify the local density of proteins. These modes are known to shift in frequency and intensity as a function of protein secondary structure and can thus help identify a protein, as well as changes in its tertiary structure (43).

Spectroscopic identification of proteins requires resolving several modes simultaneously. SINS enables spectroscopic characterization of the complete fingerprint region, which spans several hundred cm^{-1}. Fig. 5 shows SINS images (Fig. 5*A*) and spectra (Fig. 5*C*) of a dried γ-globulin protein on a Si substrate. γ-Globulin is a naturally occurring immunological protein, which, as expected, aggregates in an amorphous film upon deposition. Thickness-dependent dielectric contrast is observed over tens of nanometers, corresponding to the penetration depth of the evanescent field from the tip. Fig. 5*C* compares γ-globulin SINS $\Phi(\bar{\nu})$ spectra with a far-field FTIR spectrum of the same sample. The SINS peak positions and shapes of both the Amide I and Amide II peaks are nearly identical to far-field measurements that require averaging over a 10 × 10-μm^2 area. Several smaller peaks are also observed in the 1,200 – 1,400-cm^{-1} region, which result from the Amide III mode and the vibrations of amino acid side chains. Comparisons between γ-globulin and bovine serum albumin (BSA) (Fig. S3) reveal spectral shifts in the SINS spectra that are also observed in the far-field spectra, thus demonstrating that SINS shares the ability of far-field FTIR spectroscopy to determine both protein identity and distribution, but on the scale of tens of nanometers rather than several micrometers.

Fig. 5 also shows an SINS image (Fig. 5*B*) and spectrum (Fig. 5*C*) of a peptoid nanosheet. Peptoids, or *N*-substituted glycines, are synthetic, sequence-specific polymers that have a polypeptide backbone, but with the side chains attached to the nitrogen atom rather than to the α-carbon as in peptides. Although this synthetic

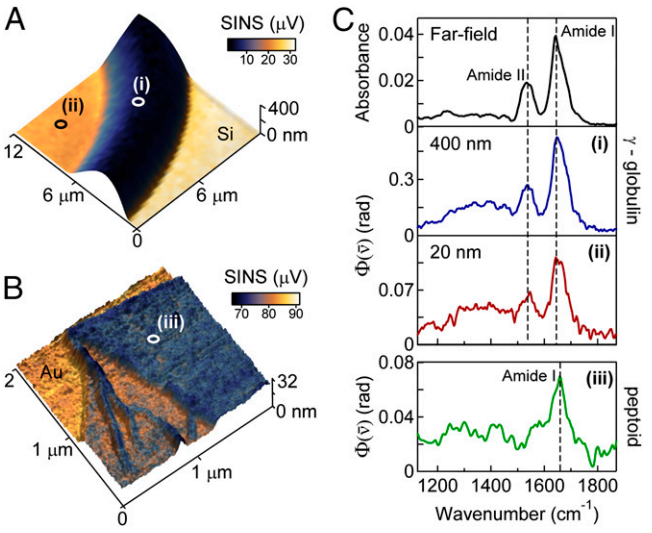

Fig. 5. High-sensitivity measurements of the fingerprint region of proteins and peptoid nanosheets. Broadband SINS images superimposed on the 3D topography of (*A*) γ-globulin dried on Si and (*B*) a peptoid nanosheet on Au. (*C*) SINS $\Phi(\bar{\nu})$ spectra of (*i*) 400-nm-thick (blue) and (*ii*) 20-nm-thick γ-globulin referenced to Si, and (*iii*) 16-nm-thick double-bilayer peptoid nanosheet (green) referenced to gold. The dashed lines are the peak positions of the Amide I and Amide II protein vibrations. The far-field absorbance spectrum of γ-globulin is shown for reference and was acquired with an IR microscope (N.A. = 0.65) using synchrotron IR radiation in transmission with a 10 × 10-μm^2 aperture centered on point *i* in *A*.

polymer is chemically similar to naturally occurring proteins, it is readily distinguished by a change in lineshape of the Amide vibrational modes. With appropriate substitution of the side chains, these engineered biopolymers self-assemble into thin, 2D nanosheets that are only 2 molecules thick (44). For the peptoid nanosheet imaged here, short peptide sequences were inserted into the nanosheet-forming peptoid polymers to form peptide loops on the nanosheet surface, effectively increasing the bilayer thickness from 3 to 8 nm (45). The integrated IR response shows sensitivity to bilayer structures, wrinkles, and folds with a spatial resolution <40 nm as measured on a bilayer edge.

Sensitivity. SINS spectra in Fig. 5*C* (*Lower*) are collected from a region of γ-globulin 20 nm in thickness and of a peptoid double bilayer ~16 nm thick. These spectral measurements of thin films and nanosheets highlight the high sensitivity of SINS, which is facilitated by the optical antenna properties of the tip (46). From the measured thickness of the film, tip radius, and resulting spatial resolution, we can estimate the amount of protein probed. Assuming an average protein density (47) of 1.4 g/cm^3, we establish that an upper bound of 150 γ-globulin protein molecules are spectroscopically probed under the area of the tip, corresponding to subzeptomole sensitivity and approximately 2×10^5 amino acid groups. A corresponding far-field synchrotron FTIR transmission microscopy analysis of the same protein sample in the same location shows that more than 8×10^5 protein molecules are required to achieve a signal-to-noise equivalent to an SINS measurement of only 150 γ-globulin protein molecules. This shows that the sensitivity of SINS exceeds that of far-field spectroscopy by more than a factor of 5,000. [With a field enhancement F ~2–3 for the Pt tips and an SINS signal intensity proportional to F^4 <100, this large improvement in sensitivity is more than can be expected by local field enhancement alone and indicates that the near-field tip–molecule mode transfer (46) is enhanced by the optical antenna effects of the tip.]

Perspective and Summary

The vibrational spectroscopic sensitivity achieved is a dramatic increase over far-field techniques and is comparable to laser-based *s*-SNOM. Although broadband IR laser source development continues, synchrotron IR radiation is currently the only source with the combined spectral irradiance, spectral coverage, and high repetition rate to measure near-field spectra over the entire mid-IR range within a single acquisition. In addition to the tip enhancement, the high sensitivity is achievable because of several advantages of the source, including minimal shot-to-shot fluctuations, high long-term power stability arising from top-off mode operations (48), and the exceptionally stable spectral distribution. These advantages enable effective signal averaging over minutes to hours, if necessary. Additional improvements to the stability of the *s*-SNOM apparatus, vibrational isolation, and mode quality of the beam are expected to further improve the sensitivity of SINS.

The broad spectral bandwidth enables more quantitative and accurate analysis of spectral position and lineshape compared with previous *s*-SNOM investigations. Real-time alignment of the interferometer before a series of scans is possible using the rapid-scan moving mirror in the interferometer, and aligning the interferometer on a resonant or nonresonant sample across the broader bandwidth ensures spectrally flat phase, improving the accuracy of the peak shape (49). Probe-induced peak shifts ranging from a few to several tens of cm^{-1} have been observed in *s*-SNOM spectra relative to far-field spectroscopies as a result of, e.g., tip–sample coupling (21, 22), tip radius (16), and the spectral phase approximation (30). Other changes to lineshape are intrinsic to the sample, however, such as spectral narrowing in a subensemble of the sample (50). Simultaneous monitoring of two or more vibrational modes with SINS will enable improved quantification of and distinction between spectral signatures intrinsic to a material sample and spectral signatures resulting from probe–sample coupling.

In summary, we have developed an IR spectroscopic method that moves broadband FTIR spectroscopy beyond the realm of diffraction-limited spectro-microscopy. The near-field confinement of IR light results in tip-limited spatial resolution 2–3 orders of magnitude smaller than the diffraction limit, and the high spectral irradiance, bandwidth, and spatial coherence of synchrotron radiation enables high signal-to-noise vibrational spectroscopy across the entire mid-IR. The chemical identity of zeptomole subensembles within a sample can unambiguously be determined by spectral features of several vibrational modes. In the case of proteins or polymer systems, this opens the possibility for not only precise chemical identification but also investigation of the protein folding state. SINS has the same benefits as far-field IR methods to obtain label-free, detailed chemical and physical information, yet with drastically improved spatial resolution and sensitivity achievable only in the near field. This highly powerful combination provides access to a form of nanochemometric analysis with the investigation of nanoscale, mesoscale, and surface phenomena that were previously impossible to study with IR techniques. Moreover, the user facility aspect of SINS makes the *s*-SNOM technique widely available to nonexperts such that it can be broadly applied to biological, surface chemistry, materials, or environmental science problems.

Materials and Methods

SINS. The ALS is a third-generation synchrotron operating in top-off mode to maintain a constant 500-mA current of 1.9-GeV electrons. Approximately 500 μW of synchrotron infrared light (700–5,000 cm^{-1}) at Beamline 5.4 is passed through a KBr beamsplitter (Thermo-Scientific) (Fig. S1, BS1). Half of the light is focused onto a platinum silicide (Nanosensors, PTSi-NCH) or platinum-coated silicon (Nanoworld, ARROW-NCPt) AFM tip with a custom parabolic mirror (N.A. ~0.4, Nutek). The other half is directed to the scanning mirror of a commercial FTIR spectrometer (Thermo-Scientific, Nicolet 6700) via a delay line. The entire system is enclosed and purged with nitrogen to remove water and carbon dioxide and to increase thermal stability. The beamsplitter (Fig. S1, BS2) of the commercial FTIR spectrometer has been customized to allow the HeNe laser to operate in its normal configuration, while having an open aperture for the synchrotron infrared beam. This modification allows the commercial instrument to operate without introducing unwanted interference artifacts into the *s*-SNOM signal. The use of the commercial FTIR spectrometer and software is advantageous because it uses the highly engineered and mature technology of traditional FTIR spectroscopy. The ability to perform rapid-scan measurements is particularly beneficial both in initial alignment and in avoiding phase drifts during a single acquisition. The rapid-scan mode can also be used to acquire low-resolution spectra simultaneously with topography. Back-scattered light and the light reflected off the moving mirror are combined on the KBr beamsplitter (Fig. S1, BS1) and focused onto an MCT detector (Kolmar KLD-0.1). To avoid saturation of the detector, a germanium wedge is used as a reflector in the delay line for the moving mirror. The double-pass arrangement allows for a reduction in signal from this arm by ~75%. The AFM (modified Innova, Bruker) is operated in noncontact mode and the tip-scattered signal is demodulated at the tip-tapping frequency (typically 250–300 kHz) with a lock-in amplifier (Zurich Instruments). Typical values of the lock-in time constant and mirror speed are ~200 μs and 0.15 cm/s, respectively, which allow for a single interferogram to be acquired in ~4 s at 4-cm^{-1} resolution. This speed can be increased up to 40 times faster at the expense of spectral resolution, signal-to-noise ratio, and/or limits on high-frequency spectral components. The demodulated signal is fed back into the commercial FTIR spectrometer and the data are acquired through commercial software (Omnic, Thermo-Scientific).

Analysis. Interferograms are postprocessed through custom programs with commercial fast Fourier transform analysis packages (Wavemetrics Igor). To remove the instrumental response from spectra, both the amplitude and phase spectra are referenced to a sample with flat spectral response, such as gold or silicon, obtaining $|A(\bar{\nu})| = |A(\bar{\nu})|_{samp} / |A(\bar{\nu})|_{ref}$ and $\Phi(\bar{\nu}) = \Phi(\bar{\nu})_{samp} - \Phi(\bar{\nu})_{ref}$. The imaginary part of the SINS signal $\mathrm{Im}(\sigma_n(\bar{\nu}))$, which is proportional to $\Phi(\bar{\nu})$ to a good approximation for not too strong oscillators and/or large broadband nonresonant responses, approximates the absorption coefficient of materials measured in traditional FTIR measurements (17, 30).

Far-Field IR Microspectroscopy. Far-field IR transmission spectra of protein samples on silicon were measured with a synchrotron-based FTIR microscope (Thermo-Scientific, Nicolet 6700 spectrometer and Continuum microscope) on Beamline 5.4 at the ALS. The synchrotron source produces a diffraction-limited spot size (N.A. = 0.65), which is about 6 μm in the region of the Amide I vibrational mode (~1,640 cm^{-1}). Spectra were averaged for 10 min and collected in the 650–4000-cm^{-1} range with 8-cm^{-1} resolution using a KBr beamsplitter and an MCT detector.

Sample Preparation. All samples were prepared on flat substrates suitable for AFM investigation and were investigated under ambient conditions. SiO_2–Si microstructures were purchased from MikroMasch (TGXYZ02), containing circular pillars of SiO_2 ~100 nm in height with a pitch of 5 μm on a flat Si substrate. The *M. edulis* shell sample was provided by Pupa Gilbert (University of Wisconsin, Madison, WI) and was prepared by cutting with a jeweler's saw and polishing with alumina grit (Master Prep). Protein samples were prepared by Sun Choi (Lawrence Berkeley National Laboratory) by a recently developed printing process (51) using a 0.1% solution of bovine γ-globulin (Sigma-Aldrich) in deionized water on a silicon substrate. Finally, peptoid loop-displaying peptoid nanosheets were prepared by Gloria Olivier (Lawrence Berkeley National Laboratory) by a previously described method (45) and dried onto a thermally evaporated gold substrate.

ACKNOWLEDGMENTS. The authors thank Gloria K. Oliver for the synthesis and provision of peptide loop-displaying peptoid nanosheets, which was performed at The Molecular Foundry (TMF), Sun Choi for providing dried protein samples, which was supported by the Berkeley Synchrotron Infrared Structural Biology (BSISB) program, and Pupa Gilbert for providing the shell sample. The authors also thank Andrew Jones and Erik Josberger for contributions to the modifications of the AFM, as well as Jaroslaw Syzdek and Benjamin Pollard for helpful discussions. The ALS and TMF are supported by the Director, Office of Science, Office of Basic Energy Sciences, and the BSISB is supported by the Office of Biological and Environmental Research, all through the US Department of Energy (DOE) under Contract DE-AC02-05CH11231. A portion of the research was supported by the US DOE, Office of Basic Energy Sciences, Division of Materials Sciences and Engineering under Award DE-FG02-12ER46893 (to E.A.M., R.L.O., and M.B.R.). Funding was provided by a partner proposal with the Environmental Molecular Sciences Laboratory, a national scientific user facility from the DOE Office of Biological and Environmental Research at Pacific Northwest National Laboratory (PNNL). PNNL is operated by Battelle for the US DOE under Contract DEAC06-76RL01830.

1. Chu MW, Chen CH (2013) Chemical mapping and quantification at the atomic scale by scanning transmission electron microscopy. *ACS Nano* 7(6):4700–4707.
2. Schmidt T, Sala A, Marchetto H, Umbach E, Freund HJ (2013) First experimental proof for aberration correction in XPEEM: Resolution, transmission enhancement, and limitation by space charge effects. *Ultramicroscopy* 126:23–32.
3. Chao W, et al. (2012) Real space soft x-ray imaging at 10 nm spatial resolution. *Opt Express* 20(9):9777–9783.
4. Huang B, Bates M, Zhuang X (2009) Super-resolution fluorescence microscopy. *Annu Rev Biochem* 78:993–1016.
5. Martin MC, Dumas P (2012) Materials sciences using synchrotron infrared light sources. *Spectrosc Prop Inorg Organomet Compd* 43:141–165.
6. Holman HYN, Bechtel HA, Hao Z, Martin MC (2010) Synchrotron IR spectromicroscopy: Chemistry of living cells. *Anal Chem* 82(21):8757–8765.
7. Marcelli A, Cricenti A, Kwiatek WM, Petibois C (2012) Biological applications of synchrotron radiation infrared spectromicroscopy. *Biotechnol Adv* 30(6):1390–1404.
8. Miller LM, Dumas P (2006) Chemical imaging of biological tissue with synchrotron infrared light. *Biochim Biophys Acta* 1758(7):846–857.
9. Carr GL (2001) Resolution limits for infrared microspectroscopy explored with synchrotron radiation. *Rev Sci Instrum* 72(3):1613–1619.
10. Mattson EC, Nasse MJ, Rak M, Gough KM, Hirschmugl CJ (2012) Restoration and spectral recovery of mid-infrared chemical images. *Anal Chem* 84(14):6173–6180.
11. Stavitski E, et al. (2013) Dynamic full-field infrared imaging with multiple synchrotron beams. *Anal Chem* 85(7):3599–3605.
12. Kazarian SG, Chan KLA (2010) Micro-and macro-attenuated total reflection Fourier transform infrared spectroscopic imaging. *Appl Spectrosc* 64(5):135A–152A.
13. Berweger S, et al. (2013) Nano-chemical infrared imaging of membrane proteins in lipid bilayers. *J Am Chem Soc* 135(49):18292–18295.
14. Huber AJ, Wittborn J, Hillenbrand R (2010) Infrared spectroscopic near-field mapping of single nanotransistors. *Nanotechnology* 21(23):235702.
15. Xu XG, Rang M, Craig IM, Raschke MB (2012) Pushing the sample-size limit of infrared vibrational nanospectroscopy: From monolayer toward single molecule sensitivity. *J Phys Chem Lett* 3(13):1836–1841.
16. Amarie S, Keilmann F (2011) Broadband-infrared assessment of phonon resonance in scattering-type near-field microscopy. *Phys Rev B* 83(4):045404.
17. Huth F, et al. (2012) Nano-FTIR absorption spectroscopy of molecular fingerprints at 20 nm spatial resolution. *Nano Lett* 12(8):3973–3978.
18. Huber R, Brodschelm A, Tauser F, Leitenstorfer A (2000) Generation and field-resolved detection of femtosecond electromagnetic pulses tunable up to 41 THz. *Appl Phys Lett* 76(22):3191–3193.
19. Calabrese C, Stingel AM, Shen L, Petersen PB (2012) Ultrafast continuum mid-infrared spectroscopy: Probing the entire vibrational spectrum in a single laser shot with femtosecond time resolution. *Opt Lett* 37(12):2265–2267.
20. Huth F, Schnell M, Wittborn J, Ocelic N, Hillenbrand R (2011) Infrared-spectroscopic nanoimaging with a thermal source. *Nat Mater* 10(5):352–356.
21. Jones AC, Raschke MB (2012) Thermal infrared near-field spectroscopy. *Nano Lett* 12(3):1475–1481.
22. Babuty A, Joulain K, Chapuis PO, Greffet JJ, De Wilde Y (2013) Blackbody spectrum revisited in the near field. *Phys Rev Lett* 110(14):146103.
23. Duncan WD, Williams GP (1983) Infrared synchrotron radiation from electron storage rings. *Appl Opt* 22(18):2914–2923.
24. Schade U, Holldack K, Kuske P, Wüstefeld G, Hübers HW (2004) THz near-field imaging employing synchrotron radiation. *Appl Phys Lett* 84(8):1422–1424.
25. Ikemoto Y, et al. (2012) Development of scattering near-field optical microspectroscopy apparatus using an infrared synchrotron radiation source. *Opt Commun* 285(8):2212–2217.
26. Hermann P, et al. (2013) Near-field imaging and nano-Fourier-transform infrared spectroscopy using broadband synchrotron radiation. *Opt Express* 21(3):2913–2919.
27. Hillenbrand R, Keilmann F (2000) Complex optical constants on a subwavelength scale. *Phys Rev Lett* 85(14):3029–3032.
28. Hillenbrand R, Knoll B, Keilmann F (2001) Pure optical contrast in scattering-type scanning near-field microscopy. *J Microsc* 202(1):77–83.
29. Birch JR (1987) Dispersive Fourier-transform spectroscopy. *Mikrochim Acta* 3(1–6):105–122.
30. Govyadinov AA, Amenabar I, Huth F, Carney PS, Hillenbrand R (2013) Quantitative measurement of local infrared absorption and dielectric function with tip-enhanced near-field microscopy. *J Phys Chem Lett* 4(9):1526–1531.
31. Zhang M, et al. (2012) Near-field spectroscopy of silicon dioxide thin films. *Phys Rev B* 85(7):075419.
32. Hillenbrand R, Taubner T, Keilmann F (2002) Phonon-enhanced light matter interaction at the nanometre scale. *Nature* 418(6894):159–162.
33. Raschke MB, Lienau C (2003) Apertureless near-field optical microscopy: Tip-sample coupling in elastic light scattering. *Appl Phys Lett* 83(24):5089.
34. Gunde MK (2000) Vibrational modes in amorphous silicon dioxide. *Physica B* 292(3–4):286–295.
35. Ordal MA, et al. (1983) Optical-properties of the metals AL, CO, CU, AU, FE, PB, NI, PD, PT, AG, TI, AND W in the infrared and far infrared. *Appl Opt* 22(7):1099–20.
36. McLeod AS, et al. (2013) Model for quantitative near-field spectroscopy and the extraction of nanoscale-resolved optical constants. arXiv:1308.1784.
37. Suzuki M, Nagasawa H (2013) Mollusk shell structures and their formation mechanism. *Can J Zool* 91(6):349–366.
38. Adler H, Kerr P (1962) Infrared study of aragonite and calcite. *Am Mineral* 47(5–6):700.
39. Amarie S, et al. (2012) Nano-FTIR chemical mapping of minerals in biological materials. *Beilstein J Nanotechnol* 3:312–323.
40. Dalbeck P, England J, Cusack M, Lee MR, Fallick AE (2006) Crystallography and chemistry of the calcium carbonate polymorph switch in M. edulis shells. *Eur J Mineral* 18(5):601–609.
41. Olson IC, et al. (2013) Crystal lattice tilting in prismatic calcite. *J Struct Biol* 183(2):180–190.
42. Amenabar I, et al. (2013) Structural analysis and mapping of individual protein complexes by infrared nanospectroscopy. *Nat Commun* 4:2890.
43. Cai S, Singh BR (1999) Identification of β-turn and random coil amide III infrared bands for secondary structure estimation of proteins. *Biophys Chem* 80(1):7–20.
44. Nam KT, et al. (2010) Free-floating ultrathin two-dimensional crystals from sequence-specific peptoid polymers. *Nat Mater* 9(5):454–460.
45. Olivier GK, et al. (2013) Antibody-mimetic peptoid nanosheets for molecular recognition. *ACS Nano* 7(10):9276–9286.
46. Olmon RL, Raschke MB (2012) Antenna-load interactions at optical frequencies: impedance matching to quantum systems. *Nanotechnology* 23(44):444001.
47. Fischer H, Polikarpov I, Craievich AF (2004) Average protein density is a molecular-weight-dependent function. *Protein Sci* 13(10):2825–2828.
48. Vernoud L, Bechtel HA, Borondics F, Martin MC (2010) Reconciling FTIR spectroscopy with top-off operations at the Advanced Light Source. *AIP Conf Proc* 1214:36–38.
49. Amarie S, Ganz T, Keilmann F (2009) Mid-infrared near-field spectroscopy. *Opt Express* 17(24):21794–21801.
50. Etchegoin PG, Le Ru EC (2010) Resolving single molecules in surface-enhanced Raman scattering within the inhomogeneous broadening of Raman peaks. *Anal Chem* 82(7):2888–2892.
51. Choi S, et al. (2012) Fast, high-throughput creation of size-tunable micro/nanoparticle clusters via evaporative self-assembly in picoliter-scale droplets of particle suspension. *Langmuir* 28(6):3102–3111.